

Cite this: *RSC Adv.*, 2017, **7**, 50680

Received 5th September 2017  
 Accepted 9th October 2017

DOI: 10.1039/c7ra09866a  
[rsc.li/rsc-advances](http://rsc.li/rsc-advances)

## Normal and abnormal dielectric relaxation behavior in $\text{KTaO}_3$ ceramics

Lei Tong, Jie Sun, Shuting Wang, Youmin Guo, Qiuju Li, Hong Wang and Chunchang Wang\*

$\text{KTaO}_3$  ceramic samples were prepared via a conventional solid state reaction route. The dielectric properties of  $\text{KTaO}_3$  were investigated in temperatures from room temperature to 1000 K and the frequency range of  $10^2$ – $10^6$  Hz. The sample exhibits an abnormal dielectric behavior contrary to the traditional thermally activated behavior in the temperature range below 450 K. Our results revealed that the sample was very sensitive to humidity, leading to a metal-insulator transition (MIT) at 473 K. It is the positive temperature coefficient of resistance of the MIT that results in the abnormal dielectric behavior. When the temperature is higher than 500 K, the sample shows two normal dielectric relaxations following thermally activated behavior. The low- and high-temperature relaxations were argued, respectively, to be related to dipolar relaxation and Maxwell–Wagner relaxations due to oxygen vacancies hopping inside grains and then being blocked by grain boundaries.

## 1. Introduction

$\text{KTaO}_3$  (KT for short) has been well-known as one of prototype incipient ferroelectric material, whose dielectric constant continuously increases with decreasing temperature and finally saturates to a plateau of  $\sim 4000$  at low enough temperatures ( $< 10$  K). This feature makes KT suitable for low-temperature applications. Due to this, a plethora of experimental and theoretical investigations have been performed on the low-temperature dielectric properties of KT.<sup>1–10</sup> Among perovskite materials, the appealing dielectric properties of low dielectric loss and relatively high dielectric permittivity for KT make it attractive for study as a promising microwave material.<sup>11–14</sup> On the other hand, KT crystal has highly polarizable lattice, which allows strong interaction of impurity-induced dipoles leading to dipole glass state<sup>15</sup> and even to ferroelectric phase transition.<sup>16,17</sup> Therefore, much attention has been paid to investigate the dielectric properties of KT induced by alien impurities.<sup>18–24</sup>

However, compared with alien defects, the ubiquitous native point defects—oxygen vacancies ( $\text{V}_{\text{Os}}$ ) are widely known to be the “culprit” for various properties of perovskite oxides.<sup>25</sup> In particular,  $\text{V}_{\text{Os}}$  are capable to induce a polarized state in KT due to lattice distortion, as reported in other perovskites.<sup>26,27</sup> Additionally, the migration and redistribution of  $\text{V}_{\text{Os}}$  have been reported to play an important role in the degradation of ferroelectric devices.<sup>7,28</sup> Therefore, fundamental knowledge of this kind of point defects in KT is of paramount importance. There are a number of theoretical reports concerning the  $\text{V}_{\text{Os}}$  in

KT.<sup>29–31</sup> In contrast to the theoretical work, only a few experimental studies on this respect were performed in thin film system.<sup>32,33</sup> To date, however, there is a notable lack of experimental work on  $\text{V}_{\text{Os}}$  in ceramic KT.

Since  $\text{V}_{\text{Os}}$  are active at high enough temperatures, we herein performed detailed investigations on high-temperature (300 to 1080 K) dielectric properties of KT ceramics aiming at understanding the dynamic features of  $\text{V}_{\text{Os}}$  in this material. We observed abnormal dielectric behavior around room temperature and two oxygen-vacancy-related dielectric relaxations at high temperatures. The mechanisms of these dielectric phenomena were discussed.

## 2. Experimental details

KT ceramic samples were prepared by the conventional solid-state reaction method as reported in ref. 34. The raw materials used in this work are  $\text{K}_2\text{CO}_3$  (99.99%),  $\text{Ta}_2\text{O}_5$  (99.99%), which were stored at 473 K for 10 h to completely remove any absorbed water. Stoichiometric powders were thoroughly mixed for 2 hours using a mortar and then calcined at 1100 K for 8 h. The resultant mixture was reground, pressed into pellets with a size of 14 mm in diameter and 1–2 mm in thickness and finally sintered at 1523 K for 2 h. Phase purity of the sintered pellets was characterized by X-ray powder diffraction (XRD) performed on a Rigaku SmartLab diffractometer (Rigaku Beijing Co., Beijing, China) with  $\text{Cu K}\alpha$  radiation. Dielectric properties in both temperature and frequency domains were measured using a Wayne Kerr 6500B precise impedance analyzer (Wayne Kerr Electronic Instrument Co., Shenzhen, China) with the sample mounted in a holder placed inside

Laboratory of Dielectric Functional Materials, School of Physics & Material Science, Anhui University, Hefei 230601, China. E-mail: [ccwang@ahu.edu.cn](mailto:ccwang@ahu.edu.cn)



a PST-2000HL dielectric measuring system (Partulab Co., Wuhan, China). The temperature domain dielectric properties were measured at fixed frequencies by varying temperature with a heating ramp of  $2\text{ K min}^{-1}$ . The frequency domain dielectric properties were measured at fixed temperatures by scanning frequency from  $10^2$  to  $10^6\text{ Hz}$ . The ac measuring signal was 100 mV. Electrodes were made by printing silver paste on both sides of the disk-type samples. Annealing treatments were performed at 1073 K for 2 h in high purity ( $>99.99\%$ )  $\text{O}_2$  or  $\text{N}_2$  with a flowing rate of  $200\text{ mL min}^{-1}$ .

### 3. Results and discussions

#### 3.1 Structure and microstructure characterization

Fig. 1 shows the typical room-temperature XRD pattern of KT ceramic sample in the  $2\theta$  range of 20 to  $80^\circ$ . The pattern can be indexed based on a cubic structure with  $\text{Pm}3\text{m}$  space group

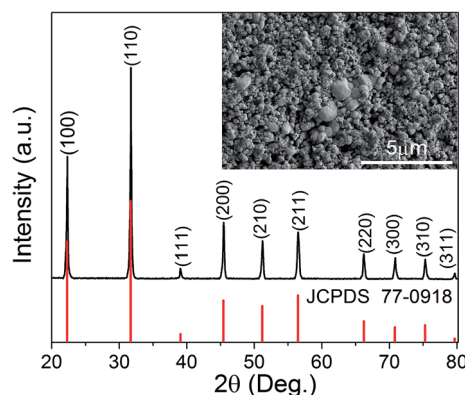


Fig. 1 The XRD pattern of the KT sample recorded at room temperature. The insert shows SEM surface morphology.

(JCPDS file no. 77-0918). No impurity phases were observed indicating the sample was identified to be single phase within the resolution of the equipment. The SEM image of the surface morphology of KT was shown in the insert of Fig. 1. It can be seen that the sample presents relatively uniform surface structure composed of particle with an average size about  $0.5\text{--}1\text{ }\mu\text{m}$  together with small pores (with the size less than  $0.5\text{ }\mu\text{m}$ ).

#### 3.2 Normal dielectric behavior of ceramic KT

Fig. 2 summarizes the dielectric properties of a same KT pellet measured in the cases of as-prepared (a–c), after being annealed in  $\text{O}_2$  (d–f), and  $\text{N}_2$  (g–i) atmospheres. In the as-prepared case, the temperature ( $T$ ) dependence of the dielectric constant,  $\epsilon'(T)$ , exhibits two weak step-wise increases as indicated by the arrows [Fig. 2(a)]. Since the step-wise increase in  $\epsilon'(T)$  is always associated with dielectric relaxation, the finding implies that there might be two relaxations in the sample. However, the dielectric loss tangent,  $\tan\delta(T)$ , shows a broad shoulder without no clear signals of relaxation [Fig. 2(b)]. This result indicates that the relaxations might be shadowed by background. In order to eliminate the background, the dielectric function of electric modulus, defined as  $M^* = M' + jM'' = 1/\epsilon^*$  is applied. It was reported that the electric modulus could effectively disclose the relaxation obscured by the background.<sup>35</sup> Fig. 2(c) shows the temperature dependence of the electric modulus. From which two dielectric regions (I and II) can be classified. In region I, owing to the absence of background, the modulus spectra,  $M''(T)$ , reveal a set of pronounced relaxation peaks. The peak position shifts to higher temperature as the measured frequency increases indicating that the relaxation follows a thermally activated behavior. In region II,  $M''(T)$  also shows a set of relaxation peaks. However, contrary to the thermally activated behavior, the peak position moves to lower

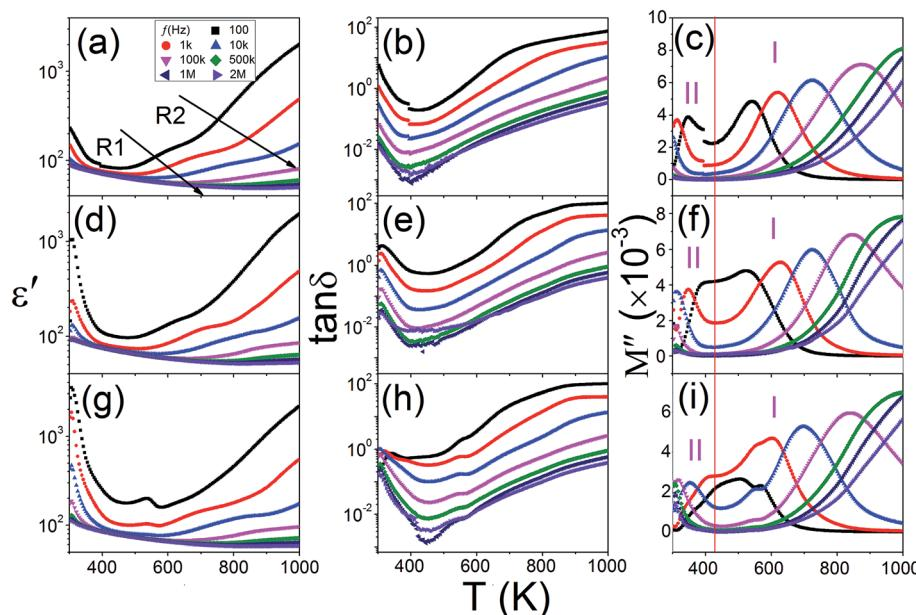


Fig. 2 The dielectric properties of KT measured in the cases of as-prepared (a–c), after being annealed in  $\text{O}_2$  (d–f), and  $\text{N}_2$  (g–i) atmospheres.



temperature as the measuring frequency increases. To clearly discuss the different dielectric behaviors, the relaxation in region I is named as normal dielectric relaxation (NDR), whereas the relaxation in region II is named as abnormal dielectric relaxation (ADR). In this section, we focus on the mechanism of the NDR. The physics of the ADR will be discussed in next section.

The NDR appears in the temperature range of  $T > 420$  K. It has been reported that relaxations in perovskites in this high temperature range are exclusively related to  $\text{V}_{\text{OS}}$ .<sup>36</sup> To clarify this point, the same pellet used in Fig. 2 was subjected to two consecutive post-annealing treatments: first in  $\text{O}_2$  and then in  $\text{N}_2$  atmospheres. After each treatment, dielectric properties were measured as a function of temperature and the results were displayed in Fig. 2(d-f) and (g-i), respectively. Although, the  $\text{O}_2$ - and  $\text{N}_2$ -treatments lead to no remarkable changes in  $\epsilon'(T)$  and  $\tan \delta(T)$ , the modulus spectra, especially for the  $\text{N}_2$ -annealed case, reveal two NDRs in region I. For brevity, the two relaxations are referred to as  $R_1$  and  $R_2$  in the order of ascending temperature. The two NDRs can be identified in the curves measured with lower frequencies, *e.g.*,  $10^2$  and  $10^3$  Hz, but can not be distinguished in the curves measured with frequency higher than 10 kHz. This indicates that the two relaxations have closed relaxation parameters. To calculate these parameters, we resort to the frequency domain.

Fig. 3(a) presents the spectroscopic plots of  $M''(f)$  measured at the temperatures ranging from 473 to 773 K with an interval of 20 K. Though the modulus spectra show a set of pronounced relaxation peaks, a careful examination reveals that the  $M''(f)$  curves are asymmetric. This is confirmed by the normalized plot as shown in Fig. 3(b), therein, the normalized electric modulus peak ( $M''/M''_{\text{max}}$ ) recorded at 573 K was plotted as a function of

the reduced temperature ( $T/T_{\text{P}}$ ) with  $M''_{\text{max}}$  and  $T_{\text{P}}$  being the peak intensity and position, respectively. It is found that the half value of full width at half maximum (FWHM) in the negative part of the peak is 0.82, which is lower than 0.93 of the positive part. This fact indicates that there still exists another weak peak in the high-frequency range, which is shadowed by the pronounced  $M''(f)$  peak. To obtain the accurate peak position, the curve of  $M''(f)$  was fitted using two Gaussian peaks. As an illustration, Fig. 3(c) shows the fitting result to the experimental data of  $M''(f)$  measured at 513 K. The measuring temperature and the peak position ( $f_{\text{P}}$ ) for both relaxations deduced from the fittings were plotted according to the Arrhenius law:

$$f_{\text{P}} = f_0 \exp(-E_a/k_{\text{B}}T) \quad (1)$$

where  $f_0$  is eigen frequency,  $E_a$  is activation energy for relaxation, and  $k_{\text{B}}$  is Boltzmann constant. Arrhenius plots for  $R_1$  and  $R_2$  (closed points) along with the linear fits (straight lines through the data points) were shown in Fig. 3(d). The relaxation parameters  $E_a$  and  $f_0$  were calculated, respectively, to be 0.83 eV and  $1.51 \times 10^{12}$  Hz for  $R_1$ , and 0.76 eV and  $6.32 \times 10^{10}$  Hz for  $R_2$ . The activation energy values for both relaxations are in the range 0.6–1.2 eV for oxygen-vacancy-related relaxations,<sup>37</sup> indicating that the two sets of NDRs in  $\text{KTaO}_3$  ceramics might be associated with the migration of  $\text{V}_{\text{OS}}$ .

It was reported that the activation energy of  $\text{V}_{\text{O}}$ -related relaxation increases (decreases) with the decreasing (increasing) concentration of  $\text{V}_{\text{OS}}$ <sup>38</sup> which can be decreased (increased) by annealing in oxygen (nitrogen). To identify this point, the relaxation parameters ( $E_a$  and  $f_0$ ) were calculated in the  $\text{O}_2$ -and then in  $\text{N}_2$ -annealed cases. Table 1 summarizes the values of the relaxation parameter of  $R_1$  and  $R_2$  in different measuring cases. From which, the values of activation energy for both relaxations are found to be increased by the  $\text{O}_2$ -annealing treatment and then decreased by the  $\text{N}_2$ -annealing treatment. This result firmly confirms that the two relaxations are associated with oxygen vacancies. The origin of  $\text{V}_{\text{OS}}$  in KT can be reasonable ascribed to be the oxygen loss during the high temperature sintering process. Because oxygen is unavoidable in perovskite oxides, especially under a high firing temperature.<sup>39</sup> Our recent results revealed that the hoping motion of  $\text{V}_{\text{OS}}$  first created a dipolar relaxation and then a Maxwell–Wagner relaxation when the vacancies were blocked by interfaces such as grain boundaries.<sup>37</sup> The observed relaxations,  $R_1$  and  $R_2$ , can be ascribed to be the dipolar relaxation inside grains and

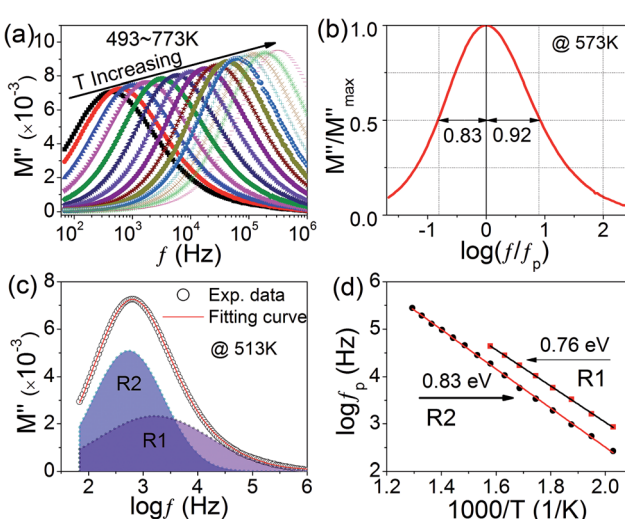


Fig. 3 (a) Frequency dependence of the imaginary part of the electric modulus for the KT from 493 to 773 K with an interval of 20 K. (b) The normalized modulus vs. the reduced frequency (in log scale) at 573 K. (c) A representative example showing the comparison between the experimental data (open circles) measured at 513 K and fitting result (solid curve) as well as the resulting peaks (dashed curves). (d) The Arrhenius plots of  $R_1$  and  $R_2$  with the solid lines being the fitting results.

Table 1 Relaxation parameters for  $R_1$  and  $R_2$  of KT measured in different annealing cases

Annealing case	$R_1$		$R_2$	
	$E_a$ (eV)	$f_0$ (Hz)	$E_a$ (eV)	$f_0$ (Hz)
As-prepared	0.76	$6.32 \times 10^{10}$	0.83	$1.51 \times 10^{12}$
$\text{O}_2$ -annealed	0.81	$5.11 \times 10^{10}$	0.89	$1.31 \times 10^{10}$
$\text{N}_2$ -annealed	0.74	$6.47 \times 10^{10}$	0.81	$1.08 \times 10^{10}$



Maxwell-Wagner relaxation due to grain boundaries, respectively. In order to evidence this point, we conduct impedance analysis.

Fig. 4(a) displays the Nyquist plot ( $Z''$  vs.  $Z'$ , where  $Z'$  and  $Z''$  are the real and imaginary parts of the complex impedance  $Z''$ ) of KT recorded at the temperatures ranging from 573 to 693 K. The complex impedance spectra were analyzed using an equivalent circuit model. Empirically, the phenomenological constant phase element (CPE), which is a capacitive element with non-Debye behavior, is used to replace the ideal capacitor with Debye behavior due to the imperfect blocking characteristics of grain boundary and/or sample-electrode interface.<sup>40,41</sup> Considering the impedance data, it can be best modeled by invoking an equivalent circuit consisting of two serially connected R-CPE units ( $R$  = resistor) shown in the inset of Fig. 4(a). The resistances of the grain and grain boundary of KT at different temperatures are obtained from the above analyses, and the results are shown in Fig. 4(b). The resistance is plotted as a function of the reciprocal temperature, and it well obeys the Arrhenius relaxation:

$$R = R_0 \exp(-E_{\text{cond}}/k_B T) \quad (2)$$

where  $R_0$  is pre-exponential term,  $E_{\text{cond}}$  is activation energy of conductivity. The liner fits based on eqn (2), shown as straight lines in Fig. 4(b), yield the activation energy 0.73 and 0.78 eV for the grain and grain boundary, respectively. These values are close but somewhat lower than those of the corresponding dielectric activation energy for  $R_1$  and  $R_2$ . This is because the fact that both relaxation and conductivity result from the same hopping process of  $V_{\text{Os}}$ , therefore both aspects have close values of activation energy. This result further demonstrates that  $R_1$  and  $R_2$  are bulk and interfacial responses, respectively.

### 3.3 Abnormal dielectric behavior of ceramic KT

To clearly evidence the abnormal dielectric behavior, detailed modulus spectra of KT in the as-prepared,  $O_2$ -, and  $N_2$ -annealed cases were measured in the temperature range from  $R_T$  to 773 K. The results were shown, respectively, in Fig. 5(a)–(c). The modulus peak in all cases was found to first shift towards low

frequency and then towards high frequency with increasing measuring temperature. Fig. 5(d) displays the Arrhenius curves for the three cases by plotting the peak position ( $f_p$ ) against the reciprocal of the measuring temperature. For the as-prepared case, a V-shaped Arrhenius curve is obtained. The data of both high- and low-temperature wings can be perfectly described by the Arrhenius law with positive and negative activation energy values indicative of NDR and ADR, respectively. In the  $O_2$ -annealed case, only one data point for ADR was seen indicating that the ADR shifts towards lower temperature range by the treatment. In the  $N_2$ -annealed case, more data point for ADR can be seen indicating that the ADR moves back to higher temperature range after  $N_2$ -annealing treatment. These results imply that the ADR is closely related to  $V_{\text{Os}}$ .

There are literally few reports on ADR behavior. To the best of our knowledge, it was first found in ferroelectric ceramic  $\text{BaTiO}_3$  (ref. 42) and addressed to be related to  $V_{\text{Os}}$  in  $\text{BaTi}_{0.85}\text{-Zr}_{0.15}\text{O}_3$  by a Japanese group.<sup>39</sup> Our group reported the ADR in laser crystals  $\text{Gd}_2\text{SiO}_5$  and Yb-doped  $\text{Gd}_2\text{SiO}_5$  and found that it was associated with a metal-insulator transition (MIT).<sup>43</sup> We pointed out that the ADR was a corollary of the positive temperature coefficient of resistance (PTCR) of the MIT. Ferroelectric ceramics exhibit PTCR effect near the ferroelectric phase transition. The PTCR effect in non-ferroelectric  $\text{Gd}_2\text{SiO}_5$  and Yb-doped  $\text{Gd}_2\text{SiO}_5$  was caused by oxygen vacancy ordering.<sup>43</sup>

To find out whether or not the ADR in KT is associated with a MIT, we performed detailed impedance analysis on KT in the as-prepared,  $O_2$ -, and  $N_2$ -annealed cases and the corresponding results are illustrated in Fig. 6(a)–(c). At the lowest measuring temperatures, one notes that the impedance spectra in the frequency range  $f > 10^3$  Hz for all cases behave as linear lines in the log-log representation. The data in the range of  $f < 10^3$  Hz depart from the linear lines indicating that leaky current resulting from relaxation occurs. This departure leads to an impedance peak which can be modeled by an equivalent circuit composed of parallelly connected  $R-C$  ( $C$  = capacitor) elements as illustrated by the set of Fig. 6(d). Based on the circuit, the imaginary part of the impedance is given by

$$Z'' = R \frac{\omega \tau}{1 + (\omega \tau)^2} \quad (3)$$

where  $\tau = RC$  is relaxation time and  $\omega = 2\pi f$  is angular frequency. Obviously, the impedance shows a peak with the intensity of  $R/2$  at  $\omega\tau = 1$ . Therefore, the resistance values at different temperatures can be deduced from the impedance spectra. Fig. 6(d) shows the temperature dependent resistance for the as-prepared,  $O_2$ -, and  $N_2$ -annealed cases. Truly, a broad peak around 473 K was observed for the as-prepared case. The resistance in the low-temperature side of the peak increases with increasing temperature indicative of the PTCR effect, which is the typical metallic behavior. Whereas in the high-temperature side of the peak, the resistance decreases with increasing temperature indicative of the negative temperature coefficient of resistance characterizing an insulating or semi-conducting behavior. Thus, the peak virtually presents an MIT process. The temperature region of MIT matches well with that

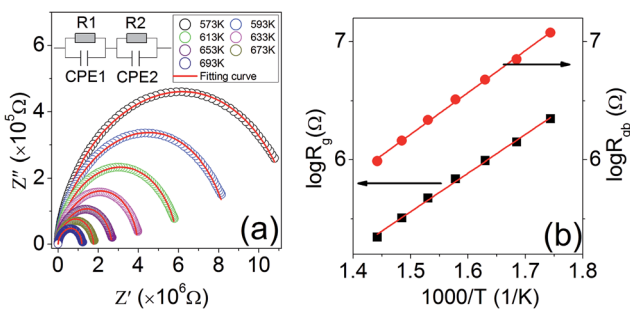


Fig. 4 (a) Complex impedance plots and corresponding fitting results (solid curves) of KT at several temperatures. The inset shows the equivalent circuits used for the fittings. (b) The Arrhenius plots for grain and grain boundary resistances deduced from the fittings. The straight lines are the linear-fitting results.

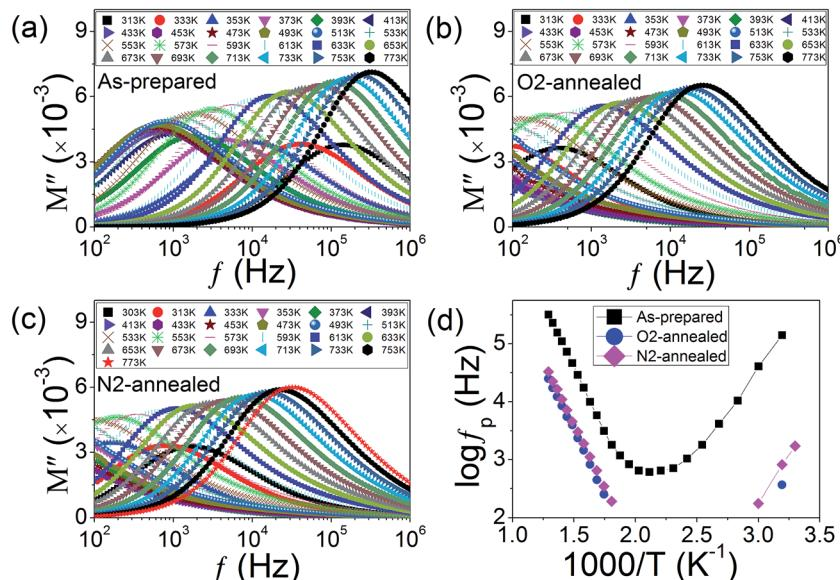


Fig. 5 The dielectric modulus spectra of KT obtained in the (a) as-prepared, (b)  $O_2$ -, and (c)  $N_2$ -annealed cases. (d) The Arrhenius curves for the three cases by plotting the peak position ( $f_p$ ) against the reciprocal of the measuring temperature.

of the ADR confirming that the present ADR is truly associated with the MIT. Although the MIT peak in the  $O_2$ -annealed case is not fully observed due to the impedance peak moving out off the lowest frequency tested [see Fig. 6(b)], it is clearly seen that the peak becomes weaker as compared to the as-prepared case. The following  $N_2$ -annealing treatment further weakens the peak. These results indicate that thermal treatments in both reducing and oxidizing atmospheres have negative influence on the MIT peak. This is contrary to the ADR caused by oxygen-vacancy ordering as reported in ref. 43. Therein, the annealing treatment in reducing (oxidizing) atmosphere enhances (weakens)

the ADR behavior in Yb-doped  $Gd_2SiO_5$  crystal. Whereas opposite annealing influence on the ADR was found in  $Gd_2SiO_5$  crystal. Therefore, a mechanism other than oxygen-vacancy ordering is responsible for the present ADR.

It is well-known that potassium (K) is a very lively and volatile metal element. The volatilisation of K during high-temperature thermal process makes K-containing oxides very sensitive to humidity.<sup>44</sup> Besides, the addition of alkali ion ( $K^+$ ) has been reported to be beneficial for improving the sensitivity of humidity.<sup>45</sup> Zhen *et al.*<sup>46</sup> pointed out that the humidity sensitivity was related to high mole content of hydrophilic group K–O

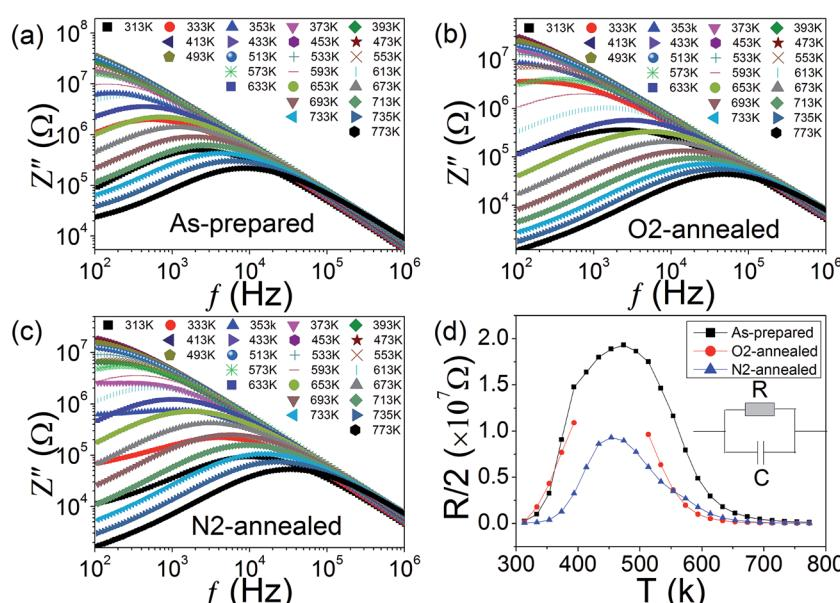


Fig. 6 The impedance spectra of KT measured at different temperatures in the (a) as-prepared, (b)  $O_2$ -, and (c)  $N_2$ -annealed cases. (d) Temperature dependence of the resistance of KT for the as-prepared,  $O_2$ -, and  $N_2$ -annealed cases. The insert shows an equivalent circuits in (d).

bonds. The addition of alkali ions could create more surface defects and oxygen vacancies, resulting in an increase of the number of adsorption sites for water molecules. This background provides a heuristic hint that water vapor might be the principal cause of the ADR in KT.

To elucidate this point, in Fig. 7 we recorded the change of electric modulus spectra at room temperature during the following consecutive processes: (1) we moved a KT pellet into the vacuum chamber of Janis SHI-4ST-1 closed cycle cryostat and started pumping, after 5 and 120 min, we recorded the frequency dependence of the modulus; (2) we opened the vacuum valve letting ambient air entering into the chamber and recorded the frequency dependence of the modulus at a series of time intervals. As seen from Fig. 7, when the sample was moved into vacuum chamber, the curve modulus almost dose not change with frequency and time. However, after exposing to ambient air, the modulus immediately shows a pronounced peak. The peak position was found to shift to high frequency with increasing exposing time. After exposing a short time of 5 min, the peak moves to low frequency with time increasing. This finding indicates that KT is very sensitive to humidity, which makes it suitable for humidity-sensitive material. After 30 min, only the high-frequency wing of the peak can be seen indicating that the peak moves out off the measuring frequency window. After 120 min, modulus spectra are independent of both time and frequency. These results firmly demonstrate that the appearance and disappearance of the electric modulus peak are related to the water adsorption and desorption in the sample, *i.e.*, the variation of surrounding humidity. It, therefore, follows that the ADR in KT is induced by water vapor.

It is noteworthy that an non-Debye dielectric relaxation caused by water vapor in porous silica glasses has been extensively investigated by the group of Feldman.<sup>47–50</sup> The non-Debye dielectric relaxation they called is actually the ADR termed herein. To describe this unusually relaxation they suggested a complicated relaxation time given by

$$\tau = \tau_0 \exp \left\{ \frac{H_a}{k_B T} + C \exp \left( - \frac{H_d}{k_B T} \right) \right\} \quad (4)$$

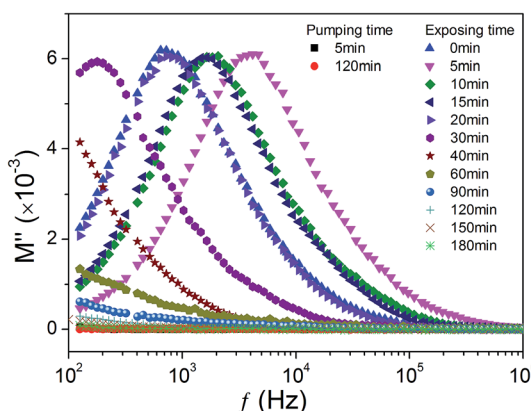


Fig. 7 The dielectric modulus spectra measured in closed vacuum chamber at room temperature during pumping and exposing processes.

where  $\tau_0$  is pre-exponential fact,  $C$  is a constant,  $H_a$  and  $H_d$  are related to activation energy and defect formation energy, respectively. The first term of eqn (4) actually presents the NDR, while the second term reflects the ADR.

To check whether or not eqn (4) works in the present case, the relaxation time was deduced from the modulus spectra in the as-prepared case as shown in Fig. 5(a). Based on the  $R$ - $C$  circuit, the modulus is given by

$$M'' = \frac{C_0}{C} \frac{\omega \tau}{1 + (\omega \tau)^2} \quad (5)$$

where  $(C_0) C$  is the (vacuum) capacitance of the measuring cell. Similar to that of the impedance, the modulus registers a peak when  $\omega \tau = 1$  is fulfill. Thus, the relaxation times at different temperatures can be deduced from the modulus peaks. Fig. 8 shows the Arrhenius plot of the deduced relaxation time. The plot can be clarified into two regions as separated by a vertical line with a boundary temperature of 473 K. In the temperature region of  $T < 473$  K, the Arrhenius plot of  $\tau$  shows positive slope indicative of ADR. Whereas in the region of  $T > 473$  K, the plot shows negative slope indicative of NDR. The fitting result based on eqn (4) was shown as solid line in Fig. 8. The fitting is not satisfactory, indicating that eqn (4) is not suitable for the present case.

As aforementioned that the ADR in non-ferroelectric materials is a corollary of PTCR effect. To decipher the relationship between the PTCR effect and ADR, the resistance data for the as-prepared KT pellet as shown in Fig. 5(a) were replotted in Fig. 8 for comparison. It is clearly seen that the temperature region of PTCR effect coincides with the ADR region. Therefore, the ADR results from the PTCR effect. This conclusion can be well understood based on the two facts: (1) since  $\tau = RC$ , the capacitance as indicated by the modulus peak [see eqn (5)] slightly increases with increasing temperature as shown in Fig. 5(a). Thus,  $C$  can be treated as temperature-independent. The relaxation time is therefore determined by  $R$ . In the PTCR region, the relaxation time increases with increasing temperature giving rise to the ADR.

Let us focus on the origin of the PTCT effect. As aforementioned that the K-containing oxides is very sensitive to humidity.

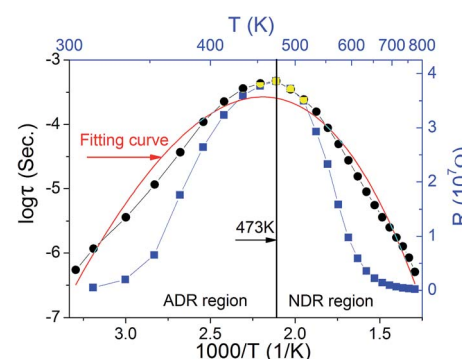


Fig. 8 Comparison between the deduced relaxation time (black circles) and the fitting result based on eqn (4) (red line) as well as the resistance for KT recorded in the as-prepared case (blue square).



Fig. 9 Ichnography illustration of the surface-layer structure of the tested cell.

When water molecules are adsorbed by  $K^+$  ions, they subsequently transfer to  $OH^-$  groups.<sup>46</sup> The tested sample then is composed of relatively conductive surface layer and more insulating inner (bulk) part as illustrated in Fig. 9. The measured resistance can be modeled by two parallelly connected resistors:  $R_b$  for the bulk part and  $R_s$  for the surface layer. Therefore, the resistance is given by:

$$1/R = 1/R_s + 1/R_b \quad (6)$$

Since  $R_s < R_b$ , the resistance is dominated by the surface layer. Based on this fact, the observed ADR can be well explained: for the results obtained by varying temperature, more and more water molecules emit out off the sample as the measuring temperature increases. Thus,  $R_s$  increases with increasing temperature leading to PTCT effect, which, in turn, creates the ADR. For the results obtained varying time as shown in Fig. 7, when the sample is exposed to air, water absorption takes place immediately resulting in the surface layer. This leads to the rapid decrease of the resistance and moves the modulus peak into the frequency window. Elongating the exposing time means enlarging the surface layer volume and area ( $A$ ), due to the adsorbed water penetrating into the inner part *via* meandering micropores. The capacitance of the surface layer given by

$$C_s = \frac{\epsilon_0 \epsilon_r A}{d} \quad (7)$$

where  $\epsilon_0$  and  $\epsilon_r$  are dielectric constants of vacuum and surface layer, respectively.  $d$  is sample thickness, which is a constant. Obviously,  $C_s$  increases with increasing exposing time. As the surface layer is formed, the sample resistance is determined by this layer and becomes temperature-dependent but time-independent. Therefore, the relaxation,  $\tau = RC$ , is mainly controlled by the capacitance and increases with increasing exposing time. This is the reason why the modulus peak moves towards lower frequency when the exposing time is longer than 5 min.

## 4. Conclusions

In summary, we reported an anomalous dielectric behavior contrary to the traditional thermally activated behavior in  $KTaO_3$  ceramics in the temperature range below 450 K. Our results indicated that the abnormal dielectric behavior was associated with a metal-insulator transition induced by humidity. In the temperature range higher than 500 K, two sets of oxygen-vacancy-related relaxations ( $R_1$  and  $R_2$ ) were observed.

The low-temperature relaxation was argued to be a dipolar relaxation caused by oxygen vacancies hopping inside grains and the high-temperature one was ascribed to be a Maxwell-Wagner relaxation due to the vacancies being blocked by grain boundaries.

## Conflicts of interest

There are no conflicts to declare.

## Acknowledgements

The authors thank financial support from National Natural Science Foundation of China (Grant No. 51502001). This work was supported in part by the Weak Signal-Detecting Materials and Devices Integration of Anhui University (Grant No. Y01008411).

## References

- 1 Z. X. Chen, X. L. Zhang and L. E. Cross, *J. Am. Ceram. Soc.*, 1983, **66**, 511.
- 2 Z. Trybuła, S. Miga, S. Łoś, M. Trybuła and J. Dec, *Solid State Commun.*, 2010, **209**, 23.
- 3 A. K. Axelsson, M. Valant and N. M. Alford, *J. Eur. Ceram. Soc.*, 2010, **30**, 941.
- 4 B. Himmetoglu and A. Janotti, *J. Phys.: Condens. Matter*, 2016, **28**, 065502.
- 5 K. Rabe, C. H. Ahn and J. M. Triscone, *Physics of ferroelectrics: a modern perspective*, Springer, Berlin, 2007.
- 6 B. Salce, J. L. Gravil and L. A. Boatner, *J. Phys.: Condens. Matter*, 1994, **6**, 4077.
- 7 G. A. Samara, *J. Phys.: Condens. Matter*, 2003, **15**, R367.
- 8 Y. Uesu, H. Yokota, J. M. Kiat and C. Malibert, *Ferroelectrics*, 2007, **347**, 37.
- 9 I. M. Smolyaninov, *J. Phys.: Condens. Matter*, 1998, **10**, 10333.
- 10 A. R. Akbarzadeh, L. Bellaiche, K. Leung, J. Iñiguez and D. Vanderbilt, *Phys. Rev. B: Condens. Matter Mater. Phys.*, 2004, **70**, 054103.
- 11 R. G. Geyer, B. Riddle, J. Krupka and L. A. Boatner, *J. Appl. Phys.*, 2005, **97**, 104111.
- 12 S. Glinšek, D. Nuzhnyy, J. Petzelt, B. Malič, S. Kamba, V. Bovtun, M. Kempa, V. Skoromets, P. Kužel, I. Gregora and M. Kosec, *J. Appl. Phys.*, 2012, **111**, 104101.
- 13 A. K. Axelsson, Y. Pan, M. Valant and N. Alford, *J. Am. Ceram. Soc.*, 2009, **92**, 1773.
- 14 A. K. Axelsson, Y. Pan, M. Valant and N. M. Alford, *J. Am. Ceram. Soc.*, 2010, **93**, 800.
- 15 B. E. Vugmeister and M. D. Glinchuk, *Rev. Mod. Phys.*, 1990, **62**, 993.
- 16 D. Rytz, A. Châtelain and U. T. Höchli, *Phys. Rev. B: Condens. Matter Mater. Phys.*, 1983, **27**, 6830.
- 17 U. T. Höchli and L. A. Boatner, *Phys. Rev. B: Condens. Matter Mater. Phys.*, 1979, **20**, 266.
- 18 S. A. Prosandeev, V. S. Vikhnin and S. E. Kapphan, *J. Phys.: Condens. Matter*, 2002, **14**, 4407–4414.



19 Z. Trybuła, S. Miga, S. Łoś, M. Trybuła and J. Dec, *Phys. Status Solidi B*, 2016, **253**, 1076.

20 G. Geneste, J. M. Kiat, H. Yokota, Y. Uesu and F. Porcher, *Phys. Rev. B: Condens. Matter Mater. Phys.*, 2010, **81**, 144112.

21 G. Geneste, J. M. Kiat, H. Yokota and Y. Uesu, *Phys. Rev. B: Condens. Matter Mater. Phys.*, 2011, **83**, 184202.

22 A. K. Axelsson, Y. Pan, M. Valant, P. M. Vilarinho and N. M. Alford, *J. Appl. Phys.*, 2010, **108**, 064109.

23 A. Levstik, C. Filipič, O. Bidault and M. Maglione, *Phys. B Condens. Matter*, 2008, **403**, 3608.

24 E. L. Venturini, G. A. Samara, V. V. Laguta, M. D. Glinchuk and I. V. Kondakova, *Phys. Rev. B: Condens. Matter Mater. Phys.*, 2005, **71**, 094111.

25 W. L. Warren, K. Vanheusden, D. Dimos, G. E. Pike and B. A. Tuttle, *J. Am. Ceram. Soc.*, 1996, **79**, 536.

26 B. Hımmetoglu and A. Janotti, *J. Phys.: Condens. Matter*, 2016, **28**, 065502.

27 B. Salce, J. L. Gravil and L. A. Boatner, *J. Phys.: Condens. Matter*, 1994, **6**, 4077.

28 R. G. Geyer, B. Riddle, J. Krupka and L. Boatner, *J. Appl. Phys.*, 2005, **97**, 104111.

29 M. Choi, F. Oba and I. Tanaka, *Phys. Rev. B: Condens. Matter Mater. Phys.*, 2011, **83**, 214107.

30 A. Shigemi, T. Koyama and T. Wada, *Phys. Status Solidi C*, 2006, **3**, 2862.

31 S. G. Kang and D. S. Sholl, *J. Chem. Phys.*, 2014, **141**, 024707.

32 D. A. Mota, Y. Romaguera-Barcelay, A. Tkach, J. Pérez de la Cruz, P. M. Vilarinho, P. B. Tavares, J. Agostinho Moreira and A. Almeida, *J. Appl. Phys.*, 2013, **114**, 034101.

33 M. Tyunina, J. Narkilahti, M. Plekh, R. Oja, R. M. Nieminen, A. Dejneka and V. Trepakov, *Phys. Rev. Lett.*, 2010, **104**, 227601.

34 A. Tkach, A. Almeida, J. Agostinho Moreira, J. Perez de la Cruz, Y. Romaguera-Barcelay and P. M. Vilarinho, *Appl. Phys. Lett.*, 2012, **100**, 192909.

35 C. C. Wang, J. Wang, X. H. Sun, L. N. Liu, J. Zhang, J. Zheng and C. Cheng, *Solid State Commun.*, 2014, **179**, 29.

36 C. C. Wang, C. M. Lei, G. J. Wang, X. H. Sun, T. Li, S. G. Huang, H. Wang and Y. D. Li, *J. Appl. Phys.*, 2013, **113**, 094103.

37 C. C. Wang, M. N. Zhang, K. B. Xu and G. J. Wang, *J. Appl. Phys.*, 2013, **112**, 034109.

38 S. Steinsvik, R. Bugge, J. O. N. Gjønnes, J. Taftø and T. Norby, *J. Phys. Chem. Solids*, 1997, **58**, 969.

39 J. Xu and M. Itoh, *Chem. Mater.*, 2005, **17**, 1711.

40 R. Schmidt, W. Eerenstein, T. Winiecki, F. D. Morrison and P. A. Midgley, *Phys. Rev. B: Condens. Matter Mater. Phys.*, 2007, **75**, 245111.

41 K. R. S. Preethi Meher and K. B. R. Varma, *J. Appl. Phys.*, 2009, **105**, 034113.

42 D. C. Sinclair and A. R. West, *J. Appl. Phys.*, 1989, **66**, 3850.

43 L. N. Liu, C. C. Wang, D. M. Zhang, Q. L. Zhang, K. J. Wang, J. Wang and X. H. Sun, *J. Am. Ceram. Soc.*, 2014, **97**, 1823.

44 C. W. Ahn, S. Y. Lee, H. J. Lee, A. Ullah, J. S. Bae, E. D. Jong, B. H. Park and I. W. Kim, *J. Phys. D: Appl. Phys.*, 2009, **42**, 215304.

45 Z. Wang, C. Chen, T. Zhang, H. Guo, B. Zou, R. Wang and F. Wu, *Sens. Actuators, B*, 2007, **126**, 678.

46 Y. H. Zhen, M. M. Wang, S. Wang and Q. Z. Xue, *Ceram. Int.*, 2014, **40**, 10263.

47 Y. Feldman, A. Puzenko and Y. Ryabov, *Chem. Phys.*, 2002, **284**, 139.

48 A. Gutina, T. Antropova, E. Rysiakiewicz-Pasek, K. Virnik and Y. Feldman, *Microporous Mesoporous Mater.*, 2003, **58**, 237.

49 A. Gutina, E. Axelrod, A. Puzenko, E. Rysiakiewicz-Pasek, N. Kozlovich and Y. Feldman, *J. Non-Cryst. Solids*, 1998, **235**, 302.

50 Y. Ryabov, A. Gutina, V. Arkhipov and Y. Feldman, *J. Phys. Chem. B*, 2001, **105**, 1845.